INTERNATIONAL JOURNAL OF CLIMATOLOGY
Int. J. Climatol. (2015)
Published online in Wiley Online Library
(wileyonlinelibrary.com) DOI: 10.1002/joc.4313

RMetS
Royal Meteorological Society

Spatial coherence of variations in seasonal extreme precipitation events over Northwest Arid Region, China

Shaoping Wang,[a,b] Fengqing Jiang[c]* and Yongjian Ding[a]

[a] *Division of Hydrology Water-Land Resources in Cold and Arid Regions, Cold and Arid Region Environmental and Engineering Research Institute, Chinese Academy of Sciences, Gansu, China*
[b] *College of Resources and Environment, University of Chinese Academy of Sciences, Beijing, China*
[c] *Xinjiang Institute of Ecology and Geography, Chinese Academy of Sciences, Urumqi, China*

ABSTRACT: Daily precipitation data covering the period of 1961–2009 from 72 stations in Northwest Arid Region, China, are analysed to investigate coherent subregions of variations in extreme precipitation events. First, four extreme precipitation indices, i.e. number of heavy precipitation days (DPh), precipitation intensity above heavy precipitation (IPh), number of torrential precipitation days (DPt), and precipitation intensity above torrential precipitation (IPt), were defined and analysed seasonally. Then rotated empirical orthogonal function (REOF) technique is used to identify the coherent subregions of these seasonal extreme precipitation indices and related trends. The results indicate that the number of coherent subregions of DPh, IPh, DPt, and IPt is 6, 5, 14, and 10 for spring; 4, 18, 6, and 6 for summer; 15, 8, 10, and 8 for autumn; and 7, 7, 2, and 5 for winter, respectively. Attribute shifts of underlying surfaces should be an important driving factor behind changes of extreme precipitation events. Intensity variations of heavy and torrential precipitation are the main reason behind significant changes of extreme precipitation, especially intensity variations of the heavy precipitation. The highest increasing magnitude of IPh is 584% $(10a)^{-1}$ which is found in summer in the west parts of the Southern Xinjiang, the middle Tianshan Mountains, and the west parts of the Junggar Basin in the Northern Xinjiang. The findings of this study are potentially relevant for the development of human understanding of hydrological cycle responses in arid regions to regional and global climate changes, particularly in terms of extreme weather extremes.

KEY WORDS spatial coherence; extreme precipitation indices; heavy and torrential precipitation thresholds; REOF; Northwest Arid Region, China

Received 2 February 2014; Revised 23 December 2014; Accepted 17 February 2015

1. Introduction

More affected by thermodynamic (e.g. convective instability) than dynamic processes (e.g. large-scale circulation) (Emori and Brown, 2005; Li *et al.*, 2011a, 2011b), extreme precipitation events are characterized by a quick, sudden onset and high intensity over relatively small geographic area, and inflict significant threats on human society worldwide such as soil erosion, landslides, mudslides, urban flash floods, traffic interruptions, casualties, huge economic losses, and so on (Thorolfsson *et al.*, 2008; Shamir *et al.*, 2013; Wu *et al.*, 2013; Zhou *et al.*, 2013). Researches show that, in the future, extreme precipitation events will increase both in intensities and frequencies at regional and global scales (Palmer and Ralsanen, 2002; Meehl *et al.*, 2005; Kharin *et al.*, 2013; Li *et al.*, 2013a, 2013b) but have significant spatial variations regionally (Costa and Soares, 2009; Feng *et al.*, 2011; Hussain and Lee, 2013; Zhang *et al.*, 2014a). However, previous researches generally focused on trends of extreme precipitation at large spatial scales (Karagiannidis *et al.*, 2012; Santo *et al.*, 2014; Zhang *et al.*, 2014b). In order to make local planning and countermeasures adapt to extreme precipitation events effectively, spatial coherence of variations in extreme precipitation events at regional scale is also necessary to be investigated and which is believed to be important for regional human mitigation to climate changes and regional water resources management.

Extreme precipitation indices (Zhang *et al.*, 2011; Jiang *et al.*, 2012; Wang *et al.*, 2013) were well introduced and defined in RClimDex Users Guide (http://etccdi.pacificclimate.org/software.shtml). However, these indices were defined by absolute threshold method or percentile threshold method and may not be suitable for analysis of precipitation extremes in regions with uneven spatial distribution of precipitation, when disaster situation is considered.

Northwest Arid Region (NAR), China (Figure 1), is located in the central of the Eurasian continent with annual average precipitation of less than 200 mm. The spatial distribution of precipitation regimes is extremely uneven in space, varying from less than 45 mm to more than 500 mm (Figure 2). Because of complicated climatic conditions, threshold values of precipitation extremes that could have

* Correspondence to: F. Jiang, Xinjiang Institute of Ecology and Geography, Chinese Academy of Sciences, Urumqi, Xinjiang 830011, China.
E-mail: jiangfq@ms.xjb.ac.cn

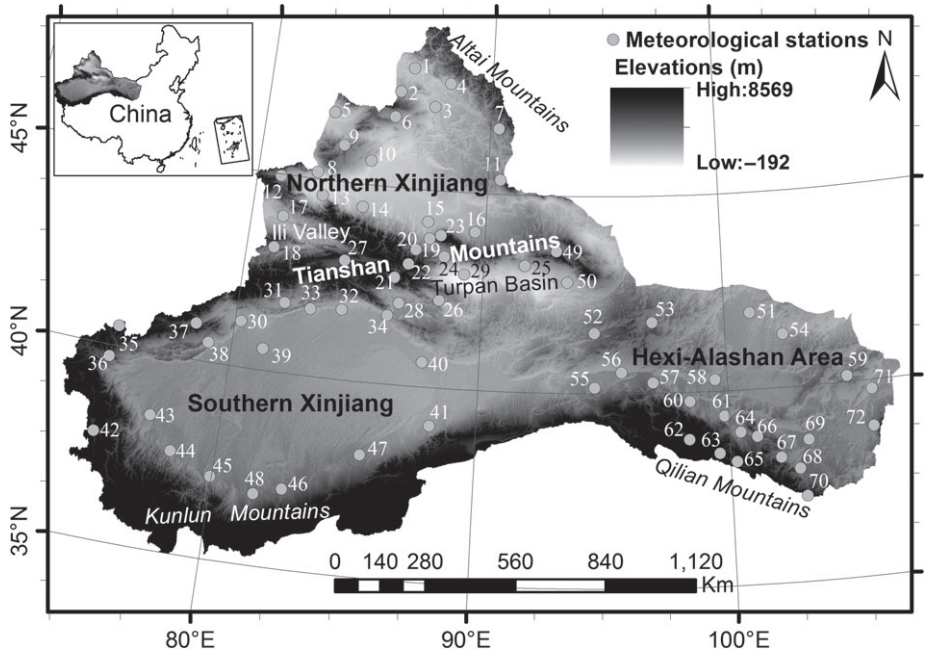

Figure 1. Locations of Northwest Arid Region, China, and meteorological stations used in this study.

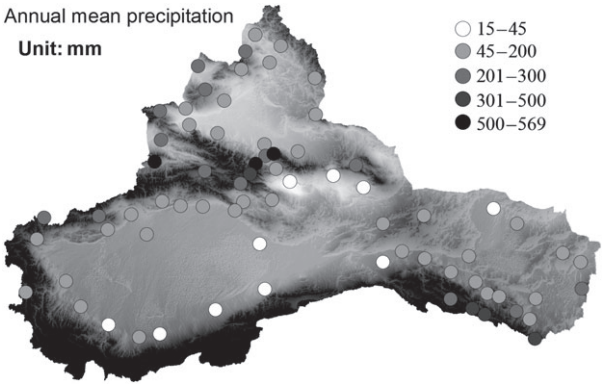

Figure 2. Spatial distribution of mean annual precipitation in Northwest Arid Region, China.

the potential to cause natural disasters are different among local areas of this region (Chen, 2012). Hence, it is improper for NAR, China, to define extreme precipitation indices using absolute threshold method, because this method ignores spatial dissimilarities of precipitation regimes. Percentile threshold method can characterize the nature of precipitation that varies significantly in space. However, it defines extreme precipitation indices just from the viewpoint of mathematical probability that ignores actual disaster situations. For some stations in NAR, China, even the 99th percentile thresholds of daily precipitation are only about 1 mm. It is improper to regard 1 mm as extreme precipitation threshold which could trigger occurrence of natural hazards. Thence, the absolute and percentile threshold methods are all not suitable for definition of extreme precipitation indices for NAR, China. In this case, a new method must be formulated to define extreme precipitation indices which can accurately quantify the extreme precipitation events in NAR, China.

In general, the objectives of this study are (1) to define extreme precipitation indices which can accurately quantify the extreme precipitation events in NAR, China; and (2) to reveal the spatial coherence of the variations in these extreme precipitation indices.

2. Data and methods

2.1. Data

The daily precipitation dataset for this study is obtained from the website of China National Meteorological Information Center (http://cdc.cma.gov.cn/dataSetDetailed.do); however, permission is required. Rigorous quality control had been conducted by China National Meteorological Information Center before the data were released. Owing to natural and anthropogenic reasons, the meteorological stations are relatively sparse and the record lengths are diverse in NAR, China. In order to keep the record lengths of the station data used in this study as uniform as possible, and the data as complete as possible, the study of this paper only analyse the precipitation series covering the period of 1961–2009 and at least 95% of the data are complete. The missing data were processed based on the methods as follows: (1) if only 1 day has missing data, the missing data are replaced by the average value of the same day in all selected years; (2) if consecutive two or more days have missing data, the missing data are processed by simple linear correlation between the station and its neighbours (distance $<$100 km) (Jiang *et al.*, 2012). Furthermore, homogenization was done for the daily precipitation dataset of these selected meteorological stations to avoid

Table 1. Precipitation intensity grading standards for the landlocked China (unit: mm day^{-1}).

Precipitation level			
Light precipitation	Moderate precipitation	Heavy precipitation	Torrential precipitation
0.1–9.9	10.0–24.9	25.0–49.9	≥50.0

the false trends caused by any anthropogenic effects. The software used to detect and adjust shifts in the time series of daily precipitation are RHtestsV3 and Rhtests_dlyPrcp (http://etccdi.pacificclimate.org/software.shtml), respectively. Finally, 72 of 83 national basic meteorological stations are selected for this study. The range of NAR, China, and the locations of the selected meteorological stations can be referred to Figure 1.

2.2. Definition of extreme precipitation indices

Heavy and torrential precipitation usually causes natural hazards and is regarded as extreme precipitation. Thus, heavy and torrential precipitation thresholds could be regarded as extreme precipitation thresholds. Heavy and torrential precipitation thresholds for the landlocked China are listed in Table 1 (http://www.igsnrr.ac.cn/kxcb/dlyzykpyd/zybk/qhzy/200610/t20061008_2155319.html). However, those for NAR, China, must be different considering situations that precipitation in this region distributes extremely uneven in space and is far less than that in the other areas of the landlocked China. Thus, precipitation intensity grading standard which is suitable for NAR, China, is needed. Chen (2012) has formulated such a standard, and it is listed in Table 2. According to Table 2, heavy and torrential precipitation thresholds for each station in NAR, China, are calculated in this study.

Because variations in the frequencies and intensities of extreme precipitation events are evidences of climate change (e.g. Hussain and Lee, 2013), based on these heavy and torrential precipitation thresholds obtained by Table 2 which are extreme precipitation thresholds for NAR, China, extreme precipitation indices showed in Table 3 are defined. Number of heavy precipitation days (DPh) and number of torrential precipitation days (DPt) can quantify frequencies of heavy and torrential precipitation events, respectively, and precipitation intensity above heavy precipitation (IPh) and precipitation intensity above torrential precipitation (IPt) can quantify intensities of them, respectively. These extreme precipitation indices were counted at the seasonal scale during the period of 1961–2009 for 72 selected stations in NAR, China. The seasons investigated are defined as follows: spring (March–May), summer (June–August), autumn (September–November), and winter (December–February).

2.3. Rotated EOF analysis

Empirical orthogonal functions (EOF), also known as principal component analysis, has been utilized as a statistical tool in the climatology since the 1950s (Kaiser, 1958). It performs an eigenvalue decomposition of the covariance matrix of the dataset and returns a low dimensional representation of the data, which are uncorrelated. However, its four inherent characteristics, i.e. domain shape dependence, subdomain instability, sampling problems, and inaccurate portrayal of the physical relationships embedded within the input matrix, hamper utility of EOF to isolate individual modes of variation (Richman, 1986). Rotated EOF analysis was therefore introduced. The theory of rotated EOF analysis and its corresponding equations were well documented by Richman (1986) and Boone *et al.* (2012).

In this study, rotated EOF analysis is used to identify coherent subregions where extreme precipitation events have similar variations. The rotational method used is VARIMAX (Kaiser, 1958). To decide how many eigenvectors (EOFs) should be retained to be rotated, the 'scree test' (Cattell, 1966; Wilks, 2006) is used with the 'eigenvalue separation rule of thumb' to separate the 'signal' from the 'noise' (North *et al.*, 1982). For 'scree test', first, the eigenvalues are sorted in descending order are plotted in a coordinate system to find the turning point on the plotted curve, and then the EOFs associated to the eigenvalues which occurs before the turning point are retained. The 'eigenvalue separation rule of thumb' is employed to test the significance of EOFs by calculating the error range of their corresponding eigenvalues. If error of neighbouring eigenvalues $|\lambda_j + 1 - \lambda_j|$ is larger than their sampling error e_j ($e_j = \lambda j \left(\frac{2}{n}\right)^{\frac{1}{2}}$, n is the sample size), the corresponding two EOFs have valuable signals and should be retained. After conducting the rotated EOF analysis, the spatial patterns and their corresponding time series are, respectively, called as Principle Component (PC) loadings and PC scores. The significance of PC loadings is tested by bootstrap method (Hellstrom and Malmgren, 2004; Dubreuil *et al.*, 2014) at the 95% confidence level. The insignificant loadings are assigned as zero. Whenever significant loadings in more than one, PC are identified at one station, the PC with the highest loading will be accepted; whenever no significant loading in any of the PCs can be detected, the station will be included in the closest region around it. Additionally, the PC loadings are also interpolated into continuous surfaces, then referring to the spatial distribution of PC loadings in the continuous surface, the stations could be divided into coherent subregions.

3. Results

3.1. Spatial distribution of new extreme precipitation indices

Spatial distribution of spring extreme precipitation indices is shown in Figure 3. DPh varies between 0 and 0.96 days, and IPh 0 and 20.44 mm day^{-1}. The largest DPh and IPh values are observed in the Tianchi region which is located in the Tianshan Mountains. While the smallest DPh and

Table 2. Precipitation intensity grading standard according to different annual precipitation (unit: mm day^{-1}) (Chen, 2012).

Annual precipitation	Precipitation level			
	Light precipitation	Moderate precipitation	Heavy precipitation	Torrential precipitation
≥500.0	0.1–9.9	10.0–24.9	25.0–49.9	≥50.0
45.0–499.9	The formula $\sqrt{\text{Annual precipitation}/500}$ is multiplied by the corresponding precipitation level criteria listed in the previous row which is for the stations whose annual precipitation are not less than 500 mm			
<45.0	0.1–2.9	3.0–7.4	7.5–14.9	≥15.0

Table 3. The rules of defining extreme precipitation indices for Northwest Arid Region, China.

ID	Indicator name	Definitions	Units
DPh	Number of heavy precipitation days	Number of days whose daily precipitation amount exceed the threshold of heavy precipitation during a period	Days
DPt	Number of torrential precipitation days	Number of days whose daily precipitation amount exceed the threshold of torrential precipitation during a period	Days
IPh	Precipitation intensity above heavy precipitation	Total precipitation of heavy precipitation during a period is divided by DPh during the same period	mm day^{-1}
IPt	Precipitation intensity above torrential precipitation	Total precipitation of torrential precipitation during a period is divided by DPt during the same period	mm day^{-1}

IPh are found mainly in the north parts of the North Xinjiang, the southeast parts of the South Xinjiang, and the east parts of NAR, China. DPt ranges between 0 and 0.22 days, and IPt between 0 and 4.65 mm day^{-1}. The largest DPt or IPt can be found in the Yutian area, and the smallest DPt or IPt can be identified mainly in the North Xinjiang, and the east parts of NAR, China.

Figure 4 shows spatial distribution of summer extreme precipitation indices. The DPh ranges between 0.1 and 2.8 days and those of IPh between 1.09 and 37.05 mm day^{-1}. The highest values of them occurs in Xiaoquzi–Daxigou areas which are located in the Tianshan Mountains, while the low values of them are generally found in the northwest parts of the North Xinjiang, the south parts of the South Xinjiang, and the central parts of NAR, China. The values of DPt are from 0 to 0.74 days, and those of IPt from 0 to 28.55 mm day^{-1}. The highest values of them are also found in the Xiaoquzi–Daxigou areas, and the low values of them generally appear in the northwest parts of the North Xinjiang, and the central parts of NAR, China.

In autumn, DPh varies between 0 and 0.55 days, and IPh between 0 and 9 mm day^{-1}. The highest values of them occurs in the Aheqi area which is located in the west parts of the South Xinjiang, and the low values of them are generally found in the north part of the North Xinjiang, the south parts of the South Xinjiang, and the central parts of NAR, China. DPt varies between 0 and 0.12 days, and IPt between 0 and 5.09 mm day^{-1}. The highest values of them are also found in the Aheqi area, and the low values of them are generally observed in the west parts of the North Xinjiang, and the central parts and the southeast parts of NAR, China (Figure 5).

For winter extreme precipitation indices, values of DPh are from 0 to 0.45 days, those of IPh are from 0 to 3.52 mm day^{-1}. The highest value of DPh is found in the Alashan plateau which is located in the east parts of NAR, China, and the highest values of IPh are not only found in the Alashan plateau but also in the Tuoli, the Alashankou, and the Alaer regions. The low values of DPh and IPh are generally found in the east parts of the Xinjiang, and the south parts of the east NAR, China. Values of DPt are from 0 to 0.12 days, and those of IPt are from 0 to 2.2 mm day^{-1}. The highest values of them are also observed in the Alaer area, and the other areas in NAR, China, are generally dominated by the low values (Figure 6).

3.2. Select EOFs to be rotated

EOFs that both pass the 'scree test' (Cattell, 1966; Wilks, 2006) and the 'rule of thumb' (North *et al.*, 1982) are retained to be rotated. For instance, scree plots of spring extreme precipitation indices (Figure 7) show that EOFs for spring DPh, IPh, DPt, and IPt should be retained as the first three, the first four, the first six, and the first seven ones, respectively, and the results are consistent with those of 'rule of thumb'. Finally, retained EOFs and their explained variances for the seasonal extreme precipitation indices are all listed in Table 4. Their accumulated variances are all not more than 70%, especially, those of summer extreme precipitation indices are all around 30%.

3.3. Coherent subregions for variations in seasonal extreme precipitation events

The extreme precipitation indices defined here for NAR, China, are proved to be in significant discrepancies in

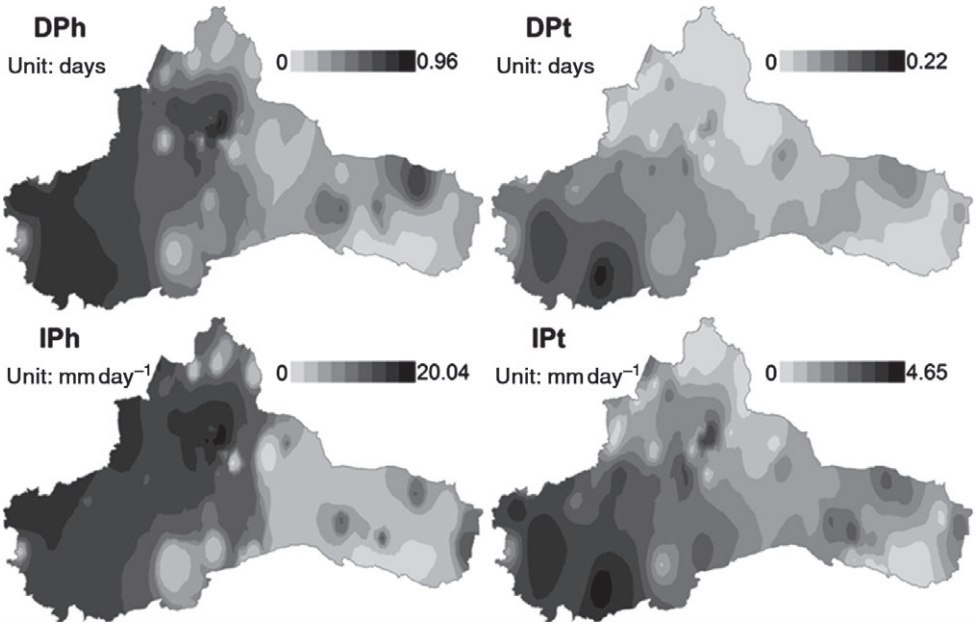

Figure 3. Spatial distribution of spring extreme precipitation indices in Northwest Arid Region, China.

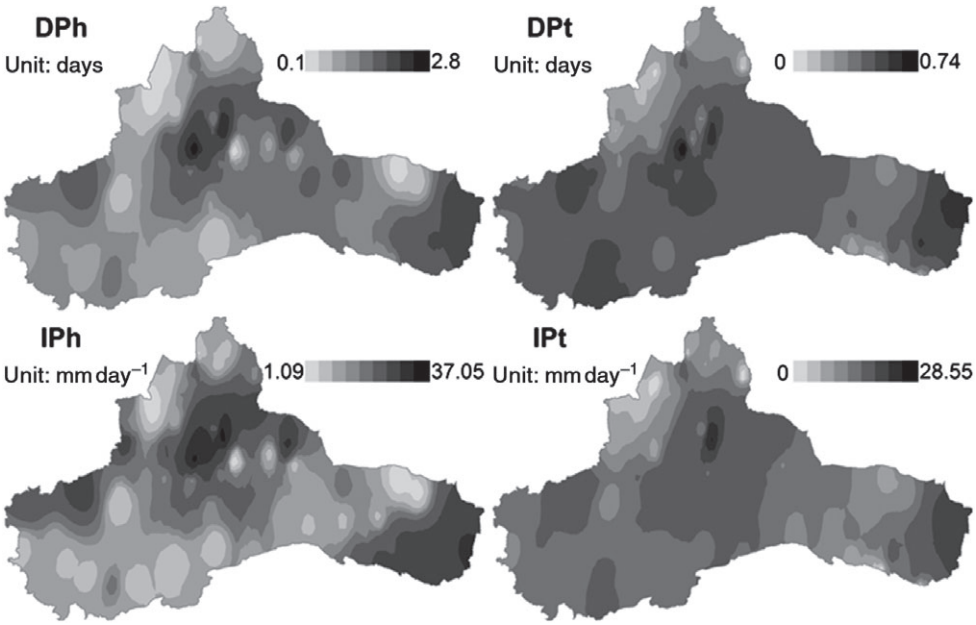

Figure 4. Spatial distribution of summer extreme precipitation indices in Northwest Arid Region, China.

space in terms of seasons in this study. The trends of these extreme precipitation indices are varying seasonally and spatially in our previous study (Wang *et al.*, 2014). Therefore, in order to better assess climate impacts and to carry out regional planning for NAR, China, identifying coherent subregions with different trends in seasonal extreme precipitation indices will be of scientific and practical merits.

3.3.1. Spring

Coherent subregions for variations of spring extreme precipitation events in NAR, China, are showed in Figure 8. It could be seen that 6, 5, 14, and 10 subregions for variations in spring DPh, IPh, DPt, and IPt are identified. Numbers of subregions of DPt and IPt are more than those of DPh and IPh.

Coherent subregions of spring DPh (Figure 8, DPh) in NAR, China, are identified mainly in the west and southwest parts of the Tianshan–Tarim Basin regions (1), the west parts of the South Xinjiang (2), the east parts of the Tianshan region (3), the west and the east parts of the Northern Xinjiang–Hexi Corridor (4), the Tengger Desert (5), and the Jaran Desert (6). Most areas of NAR, China, are dominated by increasing trend of DPh, and the highest increasing magnitude of spring DPh is 49% $(10a)^{-1}$ which is found in the subregion 3, while the

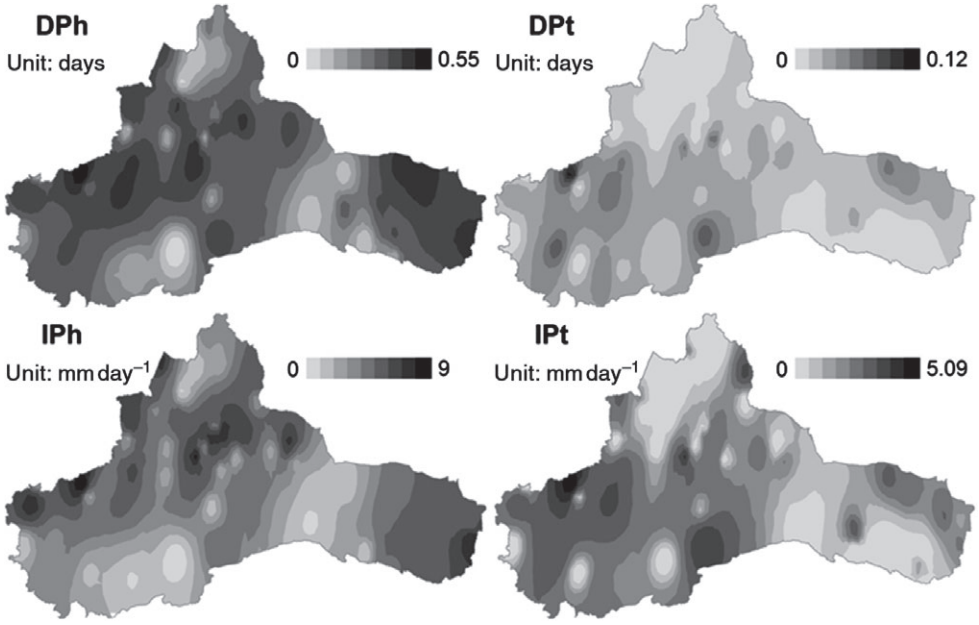

Figure 5. Spatial distribution of autumn extreme precipitation indices in Northwest Arid Region, China.

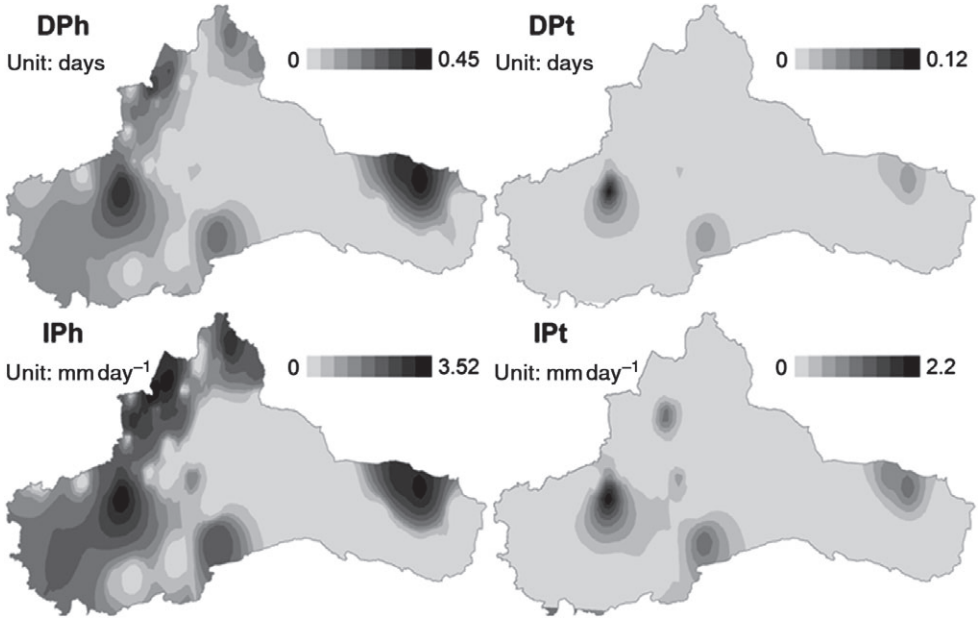

Figure 6. Spatial distribution of winter extreme precipitation indices in Northwest Arid Region, China.

spring DPh in the subregion 6 is in decreasing trend with decreasing magnitude of -49% $(10a)^{-1}$. Coherent subregions of spring IPh (Figure 8, IPh) are the Tarim Basin–Hexi Corridor (1), the west parts of the South Xinjiang–Ili Valley (2), the Wenquan–Alashankou area (3), most parts of the North Xinjiang–Alashan–Tengger Desert (4), and the Tianchi area (5). Spring IPh in most areas of NAR, China, is in increasing trend, and the highest increasing magnitude of spring IPh is 380% $(10a)^{-1}$ in the subregion 4. While the highest decreasing magnitude of -13% $(10a)^{-1}$ is observed in the subregion 3. Spatial patterns of coherent regions of spring DPt (Figure 8, DPt) and IPt (Figure 8, IPt) are similar in the North Xinjiang. However, the coherent regions of spring DPt are in relatively complicated spatial patterns when compared to those of spring IPt along the direction from the South Xinjiang to the Hexi Corridor. Coherent subregions of spring IPt are found in the west parts of the South Xinjiang (1), the western Tarim Basin (2), the eastern Tarim Basin (3), the Luntai–Kuche–Baicheng area around Middle Tianshan region (4), the Baluntai area (5), the west of Altai area–western Junggar Basin–midwest of Tianshan area (6), the eastern parts of North Xinjiang (7), the eastern Xinjiang–Hexi Corridor area (8), the east parts of the Alashan plateau (9), and the west sections of the Alashan plateau (10), with the highest increasing magnitude of

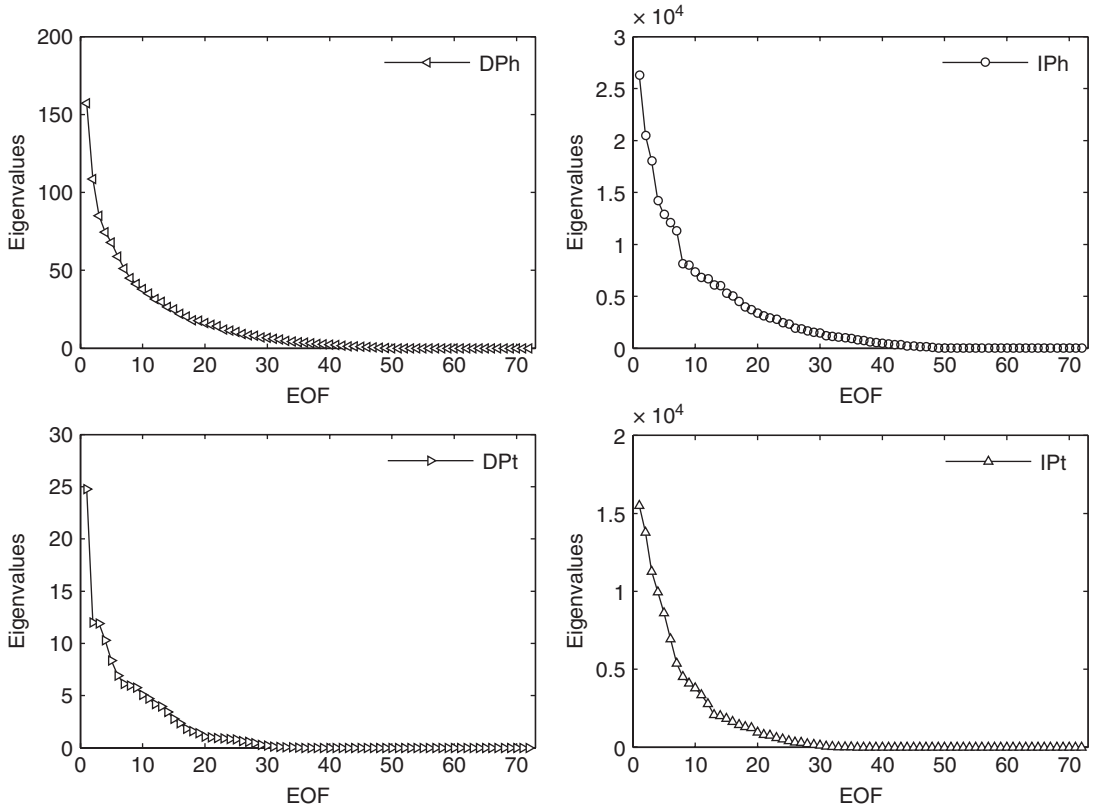

Figure 7. Change of the EOF's eigenvalues in each spring extreme precipitation index field with natural number series in Northwest Arid Region, China.

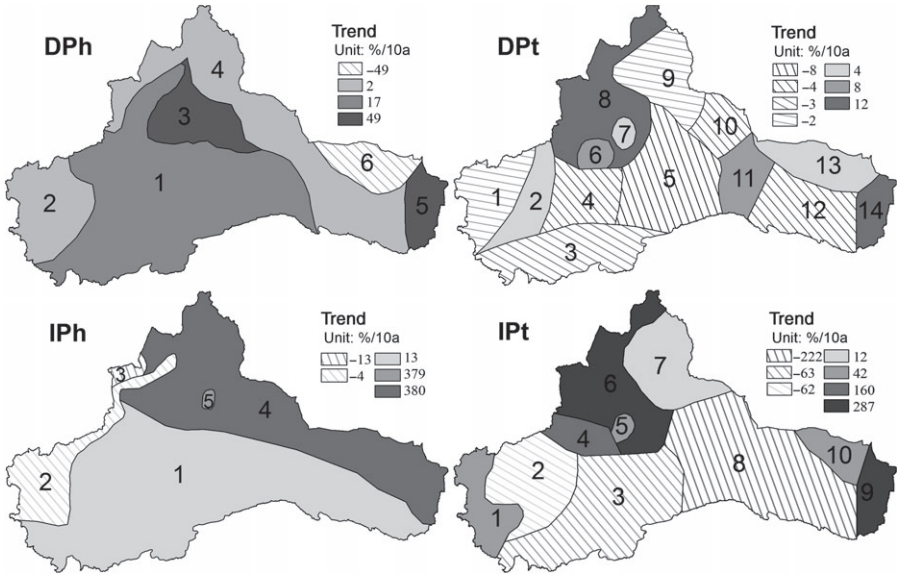

Figure 8. Coherent subregions and their related trends for the variations in spring extreme precipitation events.

287% $(10a)^{-1}$ in the subregions 6 and 9; while the highest decreasing magnitude of −222% $(10a)^{-1}$ in the subregion 8. Another four coherent subregions are identified for the spring DPt, i.e. the west (1), the middle (2), the south (3), and the east (4) parts of the Tarim Basin, the Hami area (10), the Beishan area (11), and the Hexi Corridor–Qilian Mountain area (12). The highest increasing magnitude of spring DPt is 12% $(10a)^{-1}$ in the subregions 8 and 14, while the highest decreasing magnitude of −8% $(10a)^{-1}$ is observed in the subregion 5.

3.3.2. *Summer*

There are 4, 18, 6, and 6 coherent subregions identified for summer DPh, IPh, DPt, and IPt in NAR, China, respectively (Figure 9). Number of coherent subregions of summer IPh (Figure 9, IPh) is the largest among these indices.

Table 4. EOFs of seasonal extreme precipitation indices and their associated percent of total variance and accumulated variance.

EOFs	DPh		DPt		IPh		IPt	
	Percent of total variance (%)	Percent of accumulated variance (%)	Percent of total variance (%)	Percent of accumulated variance (%)	Percent of total variance (%)	Percent of accumulated variance (%)	Percent of total variance (%)	Percent of accumulated variance (%)
Spring								
1	14.05	14.05	18.85	18.85	11.83	11.83	14.50	14.50
2	9.70	23.75	9.13	27.99	9.22	21.05	12.88	27.37
3	7.59	31.35	9.06	37.05	8.12	29.16	10.56	37.94
4			7.85	44.90	6.41	35.56	9.32	47.26
5			6.35	51.25			8.06	55.32
6			5.26	56.51			6.49	61.82
7							5.04	66.86
Summer								
1	12.15	12.15	10.37	10.37	8.55	8.55	15.64	15.64
2	9.12	21.28	8.26	18.64	7.01	15.56	9.15	24.78
3	7.25	28.53	6.56	25.20	6.06	21.62	7.15	31.93
4					5.49	27.11		
5					5.01	32.12		
Autumn								
1	10.62	10.62	12.00	12.00	11.39	11.39	16.50	16.50
2	8.87	19.49	10.08	22.08	7.46	18.85	10.19	26.69
3	7.83	27.31	8.36	30.44	6.99	25.84	9.11	35.80
4	6.78	34.09			5.71	31.56	7.32	43.12
5	5.17	39.26						
Winter								
1	39.94	39.94	45.32	45.32	21.52	21.52	30.23	30.23
2	12.58	52.52	15.88	61.20	16.07	37.58	26.05	56.28
3	9.06	61.58			11.54	49.13	13.06	69.34

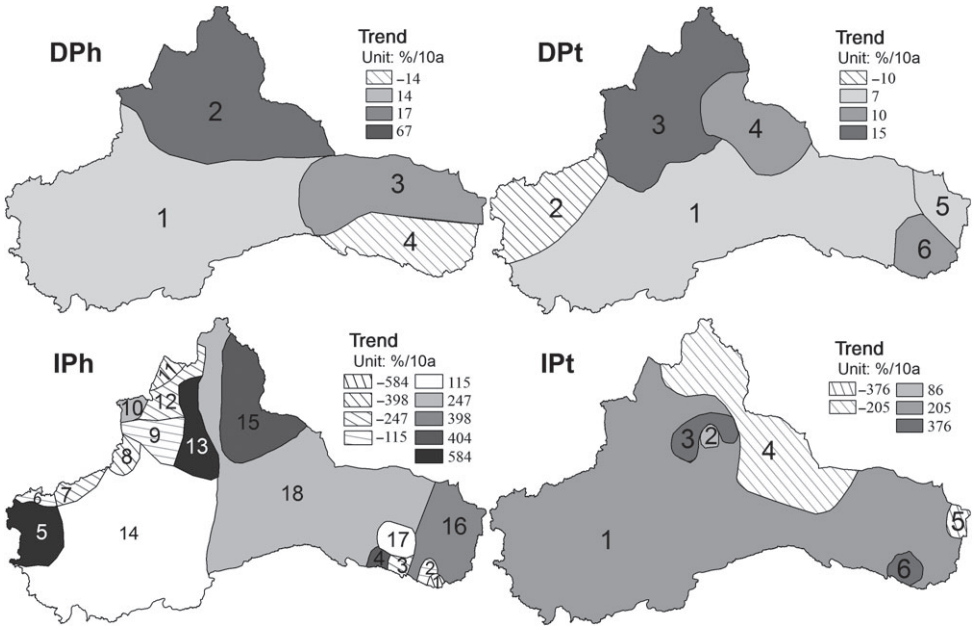

Figure 9. Coherent subregions and their related trends for the variations in summer extreme precipitation events.

There are four coherent subregions for summer DPh (Figure 9, DPh): the Tarim Basin (1), the North Xinjiang (2), the Alashan plateau (3), and the Hexi Corridor (4). Most coherent subregions of summer IPh are dominated by increasing trends and the highest increasing magnitude is 67% $(10a)^{-1}$ which is observed in the subregion 2. While only the subregion 4 is dominated by decreasing magnitude of −14% $(10a)^{-1}$. Eighteen coherent subregions for summer IPh are identified. A series of small coherent subregions scattered at the west edge of the Xinjiang and the Qilian Mountains, and most of them are in decreasing trend. The other subregions which were larger are dominated by increasing trends. The highest decreasing magnitude of −584% $(10a)^{-1}$ occurs in the

subregions 8 (the Zhaosu area) and 11 (the Tacheng area), while the highest increasing magnitude of 584% $(10a)^{-1}$ occurs in the subregions 5 (the west parts of the Southern Xinjiang) and 13 (the middle Tianshan Mountains and the west parts of the Junggar Basin in the Northern Xinjiang). Coherent subregions of the torrential precipitation events in summer are relatively fewer than those of heavy ones. In light of summer IPt (Figure 9, IPt), except the subregions 4 (a relatively large area in east parts of the North Xinjiang) and 5 (the northeast corner of the Alashan Plateau), the rest subregions of NAR, China, are all dominated by decreasing trends. The highest decreasing magnitude of −376% $(10a)^{-1}$ appears in the subregion 5, while the highest increasing magnitude of 376% $(10a)^{-1}$ occurs in the subregions 3 in the Tianshan Mountains and 6 in the Qilian Mountains. Six coherent subregions are identified for summer DPt (Figure 9, DPt) in the middle and east parts of the South Xinjiang–the west parts of the Alashan Plateau and the west edge of the Tengger Desert (1), the west parts of the South Xinjiang (2), the Tianshan–the west parts of the North Xinjiang area (3), the east parts of the North Xinjiang (4), the east parts of the Alashan Plateau (5), and the Tengger desert (6). Except the subregion 2 which is dominated by the decreasing magnitude of −10% $(10a)^{-1}$, the other subregions are all dominated by increasing trends, and the highest increasing magnitude is 15% $(10a)^{-1}$ and occurs in the subregion 3.

3.3.3. Autumn

The autumn DPh (Figure 10, DPh), IPh (Figure 10, IPh), DPt (Figure 10, DPt), and IPt (Figure 10, IPt) are classified into 15, 8, 10, and 8 coherent subregions in NAR, China, respectively, and coherent subregions of DPh and DPt are more than those of IPh and IPt.

Coherent subregions for autumn DPh are the mideast parts of the South Xinjiang (1), the west parts of the Tarim Basin (2), the Akesu–Aheqi–Keping area (3), the Zhaosu–Bayinbuluke area (4), the Yining area (5), the Wenquan area (6), the Tuoli area (7), the Tacheng–Altai area–Beitashan–the north edge of the Middle Tianshan Mountains (8), the small area in the middle of the Tianshan Mountains (9), the Hexi Corridor and its northern region (10), the Wushaoling area (11), the Tengger Desert (12), the Jaran Desert area (13), the Beishan–Ejinaqi area (14), and the east parts of the North Xinjiang (15). The subregions 3, 11, and 14 are characterized by the highest increasing magnitude of 32% $(10a)^{-1}$, while the subregions 2 and 13 are featured by the highest decreasing magnitude of −42% $(10a)^{-1}$. Spatial patterns of coherent subregions of autumn IPh are relatively compendious when compared to those of autumn DPh. The highest increasing magnitude of 391% $(10a)^{-1}$ for autumn IPh occurs in the subregion 7 (the Alashan Plateau–the Hexi Corridor), while the highest decreasing magnitude of −391% $(10a)^{-1}$ appears in the subregion 1 (the South Xinjiang). Coherent subregions of autumn DPt are the middle of South Xinjiang (1), the west parts of the Tarim Basin–the west parts of the Junggar Basin–the east parts of the Tarim Basin (2), the Keshi–the northwest parts of the Tarim Basin–the Wenquan area (3), the Alaer area (4), the Baluntai area (5), the east parts of the North Xinjiang (6), the west parts of the Aletai area–Tacheng–Hebukesaier area (7), the Guaizihu area (8), the Beishan area–the Jaran Desert Area (9), and the Hexi Corridor area (10). The highest increasing magnitude of 7% $(10a)^{-1}$ is in the subregions 3 and 10, while the highest decreasing magnitude is −7% $(10a)^{-1}$ and in the subregion 6. Eight coherent subregions for autumn IPt are the Keshi–the western edge of the Tarim Basin–the Wenquan area (1), the Alaer area (2), the central Xinjiang–the Kunlun Mountains (3), the Tianchi–the Dabancheng area (4), the Altai–the Tacheng area (5), the Altai Mountains–the Beishan area (6), the Tieganlike–bthe Ruoqiang area in the Eastern Tarim (7), and the easternNAR, China (8). The subregions 2, 5, and 8 are dominated by the highest decreasing magnitude of −144% $(10a)^{-1}$, while the autumn DPt in the subregion 1 is subject to the highest increasing magnitude of 253% $(10a)^{-1}$.

3.3.4. Winter

There are 7, 7, 2, and 5 coherent subregions identified for variations in winter DPh, IPh, DPt, and IPt in NAR, China, respectively (Figure 11). Number of coherent subregions for the heavy precipitation events is more than that for the torrential precipitation regimes. In addition, when compared to the other seasons, fewer coherent subregions are identified for winter extreme precipitation indices.

Seven coherent subregions are identified for winter DPh (Figure 11, DPh) as follows: the Ili Valley–Tarim Basin–Hexi Corridor (1), the southwest parts of the Tianshan mountains–Southern Kunlun Mountains–Altun Mountains area (2), the Alashankou–Wenquan area (3), the Tuoli area (4), the Altai Mountains–Junggar Basin–the east and west parts of the Tianshan Mountains area (5), the Beishan–Ejinaqi area (6), and the Jaran Desert area (7). The subregion 7 is characterized by the highest decreasing magnitude of −43% $(10a)^{-1}$, while the subregions 2, 3, and 6 are dominated by the highest increasing magnitude of 19% $(10a)^{-1}$. Winter IPh (Figure 11, IPh) are observed in seven coherent subregions, and three of them (the subregions 1, 5, and 6 for winter IPh) are similar with those of winter DPh (the subregions 3, 4, and 7 for winter DPh). The rest coherent subregions are different from those of winter DPh, i.e. the Kunlun Mountains–Altun Mountains–the west and east parts of the Tianshan Mountains–the east parts of the Southern Xinjiang–most parts of the Alashan Plateau–Hexi Corridor–Qilian Mountains (2), the central Tarim Basin (3), the Ili Valley–southwest parts of the Tianshan Mountains (4), and most parts of the North Xinjiang (7). In these coherent subregions, the subregion 7 are dominated by the highest increasing magnitude of 228% $(10a)^{-1}$, while the subregions 1, 3, and 6 are characterized by the highest decreasing magnitude of −315% $(10a)^{-1}$. Winter DPt (Figure 11, DPt)

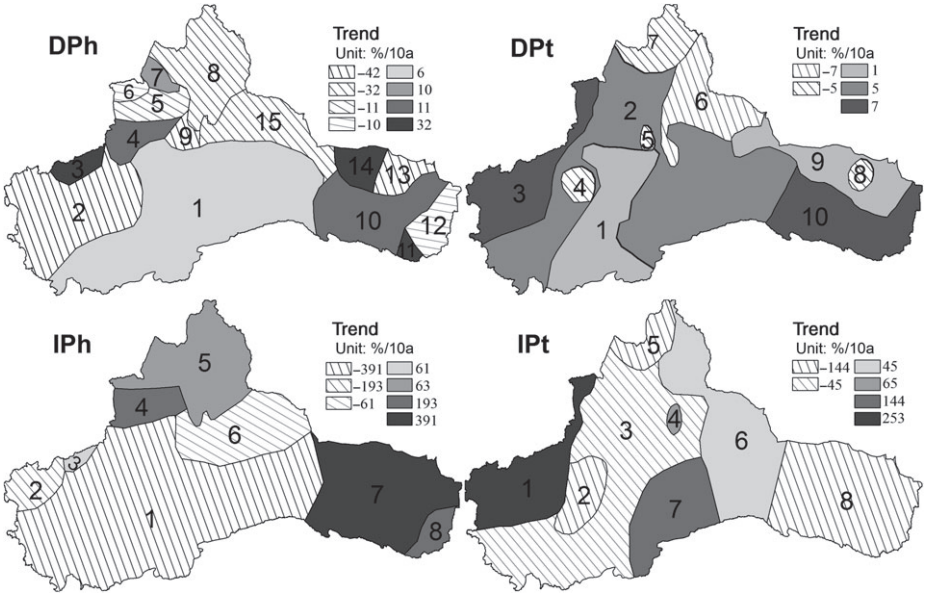

Figure 10. Coherent subregions and their related trends for the variations in autumn extreme precipitation events.

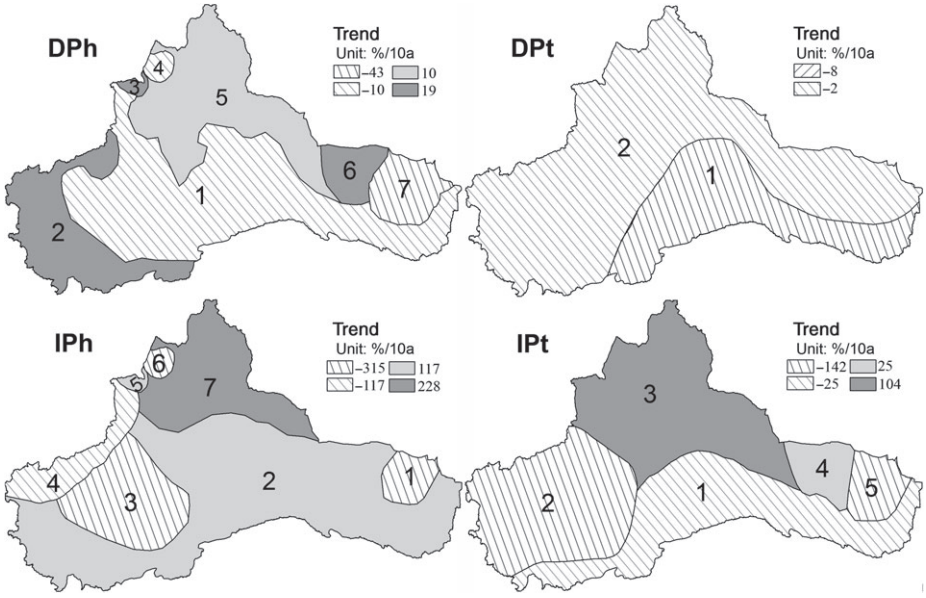

Figure 11. Coherent subregions and their related trends for the variations in winter extreme precipitation events.

are observed in two coherent subregions: the east parts of the South Xinjiang–Hexi Corridor–Qilian Mountains area (1) and the north Xinjiang–the west parts of the South Xinjiang–the Alashan Plateau area (2). Both of these two subregions are characterized by decreasing trends, and the highest decreasing magnitude is −8% $(10a)^{-1}$ and is found in the subregion 1. Winter IPt (Figure 11, IPt) is found in the similar but more regular coherent subregions when compared to the winter DPh. The subregion 3 (the Noth Xinjiang) of the winter IPt is of the highest increasing magnitude of 104% $(10a)^{-1}$; while the subregions 2 (the west parts of the south Xinjiang) and 5 (the Jaran Desert) are subject to the highest decreasing magnitude of −142% $(10a)^{-1}$ with respect to winter IPt

4. Discussions

4.1. Rationality of new extreme precipitation indices

Because the precipitation and ecological environments of the northwest China are subject to significant differences when compared to other parts of China, the local meteorological bureaus in this region defined heavy and torrential precipitation thresholds for the sake of human mitigation to natural hazards such as floods, droughts, and also other weather extremes (Chen, 2012). Chen (2012) further formulated precipitation intensity grading standard suitable for the northwest China according to annual average precipitation (Table 2), and verified its rationality. Thus, heavy and torrential precipitation thresholds calculated in this study according to

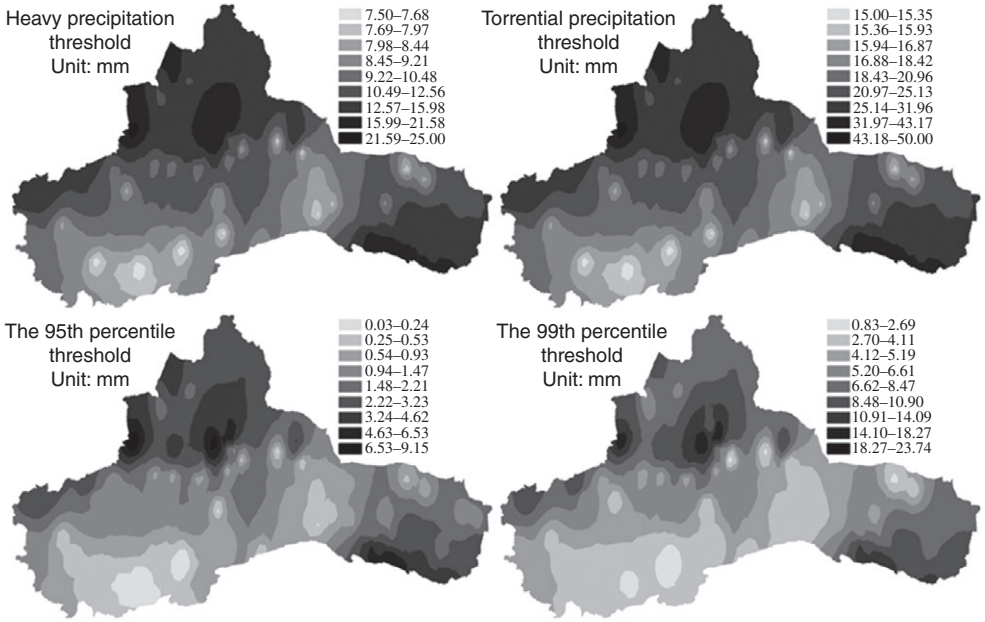

Figure 12. Spatial distribution for thresholds of the heavy and torrential precipitation, and of the 95th and 99th percentile precipitation.

Table 2 could meet disaster situations of local regions in NAR, China.

Additionally, Figure 12 shows that, like percentile thresholds, the heavy and torrential precipitation thresholds used in this study have the advantage that could characterize the nature of precipitation varying significantly in space, while percentile thresholds have differences with heavy and torrential precipitation thresholds at the same location. This implies that precipitation extremes defined by the percentile thresholds in NAR, China, cannot well mirror the actual extreme precipitation processes which have the potential to trigger natural hazards.

In summary, heavy and torrential precipitation thresholds calculated in this study are suitable for NAR, China, in depicting extreme precipitation processes. These thresholds not only have the advantage of percentile thresholds but also had the advantage of absolute thresholds that could reflect disaster situations. Thence, four new extreme precipitation indices, i.e. DPh, IPh, DPt, and IPt, defined based on these thresholds could characterize the frequencies and intensities of extreme precipitation events in NAR, China, effectively and appropriately.

4.2. Coherent subregions for variations in seasonal extreme precipitation events

Four extreme precipitation indices, DPh, IPh, DPt, IPt, are counted at the seasonal scale for daily data during the period of 1961–2009 at 72 meteorological stations in NAR, China. Spatial distribution of these extreme precipitation indices shows that extreme precipitation indices in NAR, China, are varying with the season and locations. Thus, rotated empirical orthogonal function (REOF) analysis is conducted to identify coherent subregions of variations in seasonal extreme precipitation indices.

Except winter, numbers of retained EOFs for seasonal extreme precipitation indices are generally large, and their accumulated variances are generally small. This is because climatic conditions in NAR, China, are very complicated (Chen, 2010), and it is difficult to identify large-scale circulation factors affecting the entire NAR, China. And explained variances in summer are the smallest due to the strongest convection of airflow of all seasons.

In winter, numbers of retained EOFs are relatively small, and their accumulated variances are relatively large. This is not only because of the strongest large-scale circulation in winter in NAR, China, but also because of many zero extreme precipitation indices in winter. In this study, changes of seasonal precipitation regimes are not considered, and this is the important reason behind many zero-value extreme precipitation indices in winter. In NAR, China, the precipitation types are usually snow, and under the same daily precipitation conditions, snow often causes larger disasters than rainfall. Thence, when the heavy and torrential precipitation thresholds calculated in this study are used to measure extreme precipitation events in winter, heavy snow and blizzard events are usually underestimated. Considering this situation, it is better to separately study the coherent subregions with respect to variations in extreme snow events in winter.

The accuracy of the coherent subregions identified in this study for variations in extreme precipitation events in NAR, China, is affected by the spatial density of the stations. If the precipitation data with higher space resolution could be obtained, the identified coherent subregions could be more accurate. Generally, these identified coherent subregions are basically corresponding to geomorphologic units. Thus, it could be inferred that, besides large-scale circulation background, features of underlying surfaces might be important factors relevant to the extreme precipitation events, in NAR, China.

Additionally, IPt and IPh are subject to significantly higher changing magnitude than DPt and DPh in all seasons, and those of IPh are the highest, indicating that intensity variations of heavy and torrential precipitation could be the main reason behind significant changes of extreme precipitation, especially intensity variation of heavy precipitation.

5. Conclusions

The main purpose of this study is to understand spatial coherence of the variations in seasonal extreme precipitation events in NAR, China. Extreme precipitation indices which could accurately quantify the extreme precipitation events in NAR, China, are first defined. They are DPh, IPh, DPt, and IPt. These extreme precipitation indices are counted at the seasonal scale for daily data recorded during the period of 1961–2009 at 72 meteorological stations in the NAR, China. Then REOF technique is conducted to study spatial coherence of variations in these seasonal extreme precipitation indices. The above-mentioned analysis helps to achieve the following important and interesting conclusions:

(1) The coherent subregions for variations of heavy and torrential precipitation events in NAR, China, are identified by four extreme precipitation indices defined here. The numbers of coherent subregions of DPh, IPh, DPt, and IPt were 6, 5, 14, and 10 for spring; 4, 18, 6, and 6 for summer; 15, 8, 10, and 8 for autumn; and 7, 7, 2, and 5 for winter, respectively.
(2) In spring, torrential precipitation events are more local than heavy ones, and its coherent subregions are smaller. In summer, the spatial distribution of IPh is highly complicated among four extreme precipitation indices. In autumn, more coherent subregions are identified for the variations of extreme precipitation frequencies than for those of extreme precipitation intensities. In winter, heavy precipitation events are more complex in space than torrential precipitation regimes. Generally, compared with the other seasons, fewer coherent subregions of extreme precipitation events are identified for winter than for other seasons.
(3) In all seasons, IPt and IPh are in significantly higher changing magnitude than DPt and DPh, and IPh are in the highest changing magnitude. The highest increasing magnitude of spring IPh is 380% $(10a)^{-1}$, which is found in most parts of the North Xinjiang–Alashan–Tengger Desert; of summer IPh is 584% $(10a)^{-1}$ and occurs in the west parts of the Southern Xinjiang, the middle Tianshan Mountains, and the west parts of the Junggar Basin in the Northern Xinjiang; of autumn IPh is 391% $(10a)^{-1}$ and appears in the Alashan Plateau–the Hexi Corridor, and of winter IPh is 228% $(10a)^{-1}$ which is found in most parts of the North Xinjiang. Intensity variations of heavy and torrential precipitation could be the main reason for significant change of extreme precipitation, especially intensity variation of heavy precipitation.
(4) Besides large-scale circulation background, features of underlying surfaces might be important factors relevant to the extreme precipitation events in NAR, China.

Acknowledgements

This study is financial supported by the National Natural Science Foundation of China (No. 41171378) and the Major National Scientific Research Plan of China (No. 2013CBA01800). The authors are grateful to two anonymous reviewers for their valuable comments.

References

Boone KM, McPherson RA, Richman MB, Karoly DJ. 2012. Spatial coherence of rainfall variations using the Oklahoma Mesonet. *Int. J. Climatol.* **32**: 843–853, doi: 10.1002/joc.2322.
Cattell RB. 1966. The scree test for the number of factors. *Multivariate Behav. Res.* **1**: 245–276, doi: 10.1207/s15327906mbr0102_10.
Chen X. 2010. *Physical Geography of Arid Land in China*. Science Press: Beijing (in Chinese).
Chen XY. 2012. *Studies on the Characteristics and Formative Causes of Extreme Precipitation Events in the Northern China*, MS dissertation, Lanzhou University, Lanzhou, China (in Chinese).
Costa AC, Soares A. 2009. Trends in extreme precipitation indices derived from a daily rainfall database for the South of Portugal. *Int. J. Climatol.* **29**: 1956–1975, doi: 10.1002/joc.1834.
Dubreuil S, Berveiller M, Petitjean F, Salaun M. 2014. Construction of bootstrap confidence intervals on sensitivity indices computed by polynomial chaos expansion. *Reliab. Eng. Syst. Saf.* **121**: 263–275, doi: 10.1016/j.ress.2013.09.011.
Emori S, Brown SJ. 2005. Dynamic and thermodynamic changes in mean and extreme precipitation under changed climate. *Geophys. Res. Lett.* **32**: L17706, doi: 10.1029/2005gl023272.
Feng L, Zhou TJ, Wu B, Li T, Luo JJ. 2011. Projection of future precipitation change over China with a high-resolution global atmospheric model. *Adv. Atmos. Sci.* **28**: 464–476, doi: 10.1007/s00376-010-1016-x.
Hellstrom C, Malmgren BA. 2004. Spatial analysis of extreme precipitation in Sweden 1961–2000. *Ambio* **33**: 187–192.
Hussain MS, Lee S. 2013. The regional and the seasonal variability of extreme precipitation trends in Pakistan. *Asia-Pac. J. Atmos. Sci.* **49**: 421–441, doi: 10.1007/s13143-013-0039-5.
Jiang FQ, Hu RJ, Wang SP, Zhang YW, Tong L. 2012. Trends of precipitation extremes during 1960–2008 in Xinjiang, the Northwest China. *Theor. Appl. Climatol.* **111**: 133–148, doi: 10.1007/s00704-012-0657-3.
Kaiser HF. 1958. The varimax criterion for analytic rotation in factor analysis. *Psychometrika* **23**: 187–200.
Karagiannidis AF, Karacostas T, Maheras P, Makrogiannis T. 2012. Climatological aspects of extreme precipitation in Europe, related to mid-latitude cyclonic systems. *Theor. Appl. Climatol.* **107**: 165–174, doi: 10.1007/s00704-011-0474-0.
Kharin VV, Zwiers FW, Zhang X, Wehner M. 2013. Changes in temperature and precipitation extremes in the CMIP5 ensemble. *Clim. Change* **119**: 345–357, doi: 10.1007/s10584-013-0705-8.
Li HM, Feng L, Zhou TJ. 2011a. Multi-model projection of July-August climate extreme changes over China under CO_2 doubling. Part I: precipitation. *Adv. Atmos. Sci.* **28**: 433–447.
Li HM, Feng L, Zhou TJ. 2011b. Multi-model projection of July-August climate extreme changes over China under CO_2 doubling. Part II: temperature. *Adv. Atmos. Sci.* **28**: 448–463.
Li JF, Zhang Q, Chen YD, Xu CY, Singh VP. 2013a. Changing spatiotemporal patterns of extreme precipitation regimes in China during 2071–2100 based on Earth system models. *J. Geophys. Res.* **118**: 12537–12555.
Li JF, Zhang Q, Chen YD, Xu CY, Singh VP. 2013b. GCMs-based spatiotemporal evolution of climate extremes during the 21st century in China. *J. Geophys. Res.* **118**: 11017–11035.
Meehl GA, Arblaster JM, Tebaldi C. 2005. Understanding future patterns of increased precipitation intensity in climate model simulations. *Geophys. Res. Lett.* **32**: L18719, doi: 10.1029/2005gl023680.

North GR, Bell TL, Cahalan RF, Moeng FJ. 1982. Sampling errors in the estimation of empirical orthogonal functions. *Mon. Weather Rev.* **110**: 699–706.

Palmer TN, Ralsanen J. 2002. Quantifying the risk of extreme seasonal precipitation events in a changing climate. *Nature* **415**: 512–514, doi: 10.1038/415512a.

Richman MB. 1986. Rotation of principal components. *J. Climatol.* **6**: 293–335.

Santo FE, Ramos AM, de Lima MIP, Trigo RM. 2014. Seasonal changes in daily precipitation extremes in mainland Portugal from 1941 to 2007. *Reg. Environ. Change* **14**: 1765–1788.

Shamir E, Georgakakos KP, Murphy MJ. 2013. Frequency analysis of the 7–8 December 2010 extreme precipitation in the Panama Canal Watershed. *J. Hydrol.* **480**: 136–148.

Thorolfsson ST, Rishot LP, Nilsen O, Ellingsson A, Kristiansen V, Hagen Ø, Karlsen E. 2008. Extreme rainfalls and damages on August 13 2007 in the City of Trondheim, Norway. Paper presented at the *XXV Nordic Hydrological Conference Northern Hydrology and its Global role*, Reykjavik, Iceland.

Wang HJ, Chen YN, Chen ZS. 2013. Spatial distribution and temporal trends of mean precipitation and extremes in the arid region, northwest of China, during 1960–2010. *Hydrol. Process.* **27**: 1807–1818.

Wang SP, Jiang FQ, Wu XB, Hu RJ. 2014. Temporal and spatial variability of extreme precipitation indices over Northwest Arid Region, China, from 1961 to 2010. *J. Glaciol. Geocryol.* **36**(2): 318–326, doi: 10.7522/j.issn.1000-0240.2014.0040 (in Chinese).

Wilks DS. 2006. *Statistical Methods in the Atmospheric Sciences*. International Geophysics Series, Vol. 59, 2nd edn. Academic Press: Burlington, MA.

Wu PM, Arbain AA, Mori S, Hamada J, Hattori M, Syamsudin F, Yamanaka MD. 2013. The effects of an active phase of the Madden-Julian oscillation on the extreme precipitation event over Western Java Island in January 2013. *Sola* **9**: 79–83, doi: 10.2151/sola.2013-018.

Zhang Q, Xu CY, Chen XH, Zhang ZX. 2011. Statistical behaviors of precipitation regimes in China and their links with atmospheric circulation 1960–2005. *Int. J. Climatol.* **31**: 1665–1678.

Zhang KX, Pan SM, Cao LG, Wang Y, Zhao YF, Zhang W. 2014a. Spatial distribution and temporal trends in precipitation extremes over the Hengduan Mountains region, China, from 1961 to 2012. *Quatern. Int.* **349**: 346–356.

Zhang Q, Xiao M, Singh VP, Chen YD. 2014b. Max-stable based evaluation of impacts of climate indices on extreme precipitation processes across the Poyang Lake basin, China. *Glob. Planet. Change* **122**: 271–281.

Zhou TJ, Song FF, Lin RP, Chen XL, Chen XY. 2013. Explaining extreme events of 2012 from a climate perspective. *Bull. Am. Meteorol. Soc.* **94**: S1–S74, doi: 10.1175/BAMS-D-13-00085.1.

